30th Symposium on Naval Hydrodynamics
Hobart, Tasmania, Australia, 2-7 November 2014

Simulation-Based Analysis of Hull-Propeller Interaction for a Single-Screw Transport Ship

M. Liefvendahl[1,2], R.E. Bensow[2]
([1]Swedish Defence Research Agency, FOI, [2]Chalmers University of Technology, Sweden)

ABSTRACT

The hull-propeller interaction of a single-screw transport ship is investigated in model scale using large-eddy simulation. The analysis is focused on the unsteady effective wake and its impact on the propeller. For the configuration under study, there is a significant flow separation upstream of the propeller which influences the operation. A complete geometrical model of the propeller is included in the simulations using two different computational techniques (dynamic grids and sliding interfaces respectively). Computed quantities include the time-resolved thrust, torque and side forces on the propeller, as well as the load on individual blades. The simulated unsteady flow field in the stern region and around the propeller blades is studied in detail. Results are also provided for the pressure fluctuations on the hull above the propeller. Comparison with experimental measurements is carried out both for the flow field and forces on the propeller. Furthermore, results are presented for the towed hull (without propulsion) and the propeller in open-water condition, and the hydrodynamic differences between the conditions are analysed. A discussion is included concerning the important difference between the actual (instantaneous) environment the propeller operates in and the averaged flow which typically is used as input in the design process.

INTRODUCTION

A detailed understanding of the hydrodynamics of hull-propeller-rudder interaction is of primary importance for propulsion system design. The two most important objectives in the design of marine propulsors are most often high propulsive efficiency and low levels of vibrations and noise. Depending on vessel type, the related requirement on cavitation-free speed may also have a high priority. For cargo vessels, propulsive efficiency is typically most important, but induced vibrations and noise cannot be ignored during the design procedure. For military vessels on the other hand, in particular submarines, very high priority is given to minimizing the vibrations and noise, but the propulsive efficency must naturally also be taken into account. Traditionally, this is assessed through model tests or, to an increasing degree, RANS computations. Although the former naturally includes the transient flow field involved in the interaction, it has normally been considered to be sufficient to take averaged flow quantities into account in the design process.

With the continually increasing computational capacity, RANS computations for design purposes are today more and more becoming feasible to perform in full scale, making significant improvements possible in vessel design and power prediction. However, the assessment regarding induced vibrations and noise using RANS is limited, since it is based on the average flow field. As will be elucidated in detail in the present paper, the operating environment for the propeller is instantaneously very different from the average conditions. To reliably assess these issues, the full transient flow needs to be considered, which is becoming possible today with large-eddy simulation (LES) techniques, at least in model scale. Although such simulations generally are too costly for an iterative design procedure, we find that performing this type of analysis greatly improves the understanding of the flow and will contribute in the design of a well performing vessel.

In the present study, we provide an analysis of the hydrodynamic hull-propeller-rudder interaction for a 7000 DWT (Dead-weight tonnage) chemical tanker, which has been investigated within the framework of an EU-project (see below). The tanker is fitted with one four-bladed propeller and a standard spade rudder. The analysis presented in this paper is mainly based on two large-eddy simulations of the ship in self-propulsion, including the rudder and a complete geometrical model for the rotating propeller. Cavitation modelling is not included and the water surface is approximated with a symmetry plane at the nominal water line. The hull-propeller simulations are complemented by simulations of the towed hull condition and the propeller in open water. The simulations have been carried out in model scale and in slightly different conditions and computational configurations due to different objectives within the research project, giving us the opportunity to study both differences and common traits

in the two conditions. Using LES, we can study the time-resolved quantities related to this flow, their origin and their implications on operation of the propulsor system. The individual blade loads are analysed and we find a significant variation around an average due to the unsteady wake behaviour. Although an unsteady RANS simulation would include the basic varying blade loading, the representation of the flow over the hull would be steady and the wake inflow to the propeller smooth, with the transient behaviour induced only by the propeller. The LES thus provides far better possibilities to correctly assess propeller induced vibration and noise, as well as the hydrodynamic properties of the aft ship design and the propeller operating conditions in order to achieve best performance.

The simulation results are compared with experimental data for a range of quantities including flow separation, mean velocity distribution in a cross plane fore the propeller and between the propeller and the rudder, and the hull pressure fluctuations measured on the hull above the propeller. Furthermore, the hull in isolation, as well as the propeller in open-water condition, have been studied using the same methodologies, and the results compared with those obtained in experiments of the corresponding configurations.

The paper is organised as follows. We begin by introducing the hull-propeller configuration and the operating conditions used for this study. We then present the computational methodologies used for the simulations, including some details on the treatment of propeller rotation and mesh generation. In the result sections that follow, we first analyse the flow around the towed hull, studied with the three objectives to; (i) understand the main hull flow characteristics governing the conditions for the propeller operation; (ii) allow for a rudimentary mesh sensitivity study, too costly to perform for the self-propulsion condition; and (iii) compare the simulated flow with experimental data. Following that, we briefly present a simulation of the propeller in open water conditions for the same operating point as in one of the self-propelled simulations. Finally we perform a detailed analysis of the fluid dynamics of the hull-propeller interaction, the resulting propeller forces and individual blade loading, comparing with the open-water condition, and present the resulting hull pressure fluctuations.

THE STREAMLINE TANKER

The configuration investigated here is a 7000 DWT chemical tanker of a standard design, similar to modern vessels but this particular hull has not been built in full scale. It is a single screw vessel, driven by a fixed pitch four-bladed propeller, which has been investigated within the framework of the EU-project STREAMLINE[1]. All results in the present paper have been obtained in model scale. The main hull particulars are given in Table 1, and the hull and propeller are visualised in Figure 1.

In project STREAMLINE, the flow around the tanker was investigated both for a baseline configuration, as is the case in this work, but an extensive campaign was also performed where hull and propeller were optimised and several different energy saving devices were designed for the vessel, including both pre- and post-swirl devices. Experiments have been performed both at CNR-INSEAN[2] and at CTO[3]. We will in this paper primarily refer to the CNR-INSEAN experiments. For this experimental campaing, the model was tested in the towing tank for resistance prediction and in the large circulating water channel for measuring the wake field by LDV in self propulsion conditions, as well as making cavitation observations and hull pressure measurements. The open water characteristics of the propeller was also measured in the towing tank. Published work from these studies are primarily the experimental study on propulsor-hull interaction by Pecoraro et al. (2013) for the baseline configuration and (primarily numerical) studies on the extended configurations, e.g. Deng et al. (2013), Queutey et al. (2013), Van der Ploeg and Foeth (2013), Calcagni et al. (2014).

Table 1: Main model scale dimensions of the configuration (length scale factor $\lambda = 16.5$).

Quantity	Notation	Value
Length between perpendiculars	L_{PP}	5.697 m
Beam overall	B	0.935 m
Draft	T	0.364 m
Wetted surface	S_0	8.335 m^2
Propeller diameter	D_p	0.233 m
Rudder span	R_s	0.247 m
Rudder chord	R_c	0.145 m

Results from two hull-propeller simulations, denoted HP1 and HP2 respectively, are reported in the present paper. They were performed with different objectives within STREAMLINE, and thus show a slight variation in operating conditions, as indicated in Table 2. By Froude scaling, the full-scale speed is given by, $V_0^{(f)} = \sqrt{\lambda} V_0$. The case HP1 corresponds to a speed of the full-scale vessel of 12.6 knots (at Fn $= 0.21$), which is a slow steaming condition, with zero trim and sinkage. The case HP2 corresponds to a full scale speed of 14.0 knots (at Fn $= 0.24$), which is the design speed. The sinkage for HP2 corresponds to the design value but the trim is off-design with 0.2° bow up, instead of the 0.2° bow down (which was

[1]Grant agreement 233896, European Union 7th Framework Programme.
[2]Istituto nazionale per studi ed esperienze di architettura navale, Italy.
[3]Centrum Techniki Okretowej S.A., Poland.

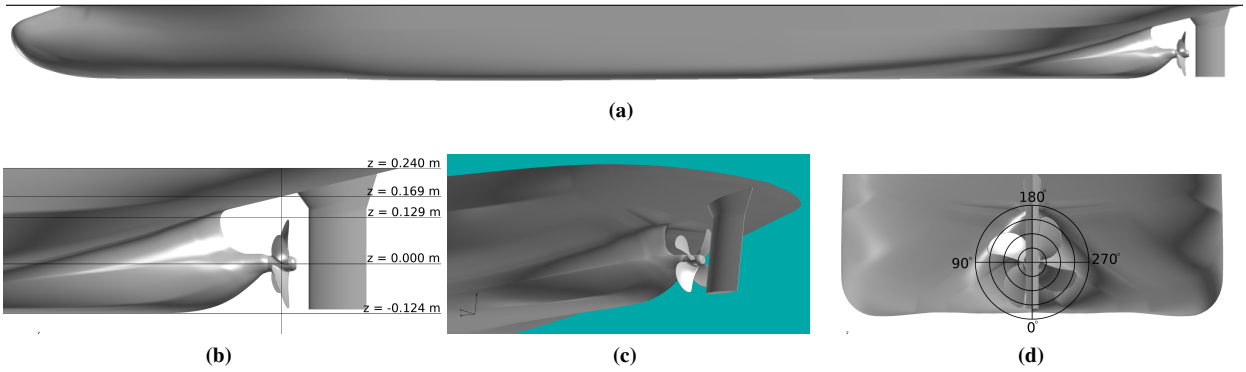

Figure 1: The STREAMLINE tanker and propeller. (a) Side view. (b) Zoom in the stern regions, with coordinates of the propeller plane and a number of vertical planes indicated. (c) Perspective view of the stern. (d) Rear view, which also illustrates the definition of the angle, φ, used to indicate the position of the propeller blades.

measured in the design condition in the towing tank). The propeller rotational speed, as well as environmental conditions, corresponds to measured values at self-propulsion in the circulating water channel at CNR-INSEAN.

Table 2: Operational parameters for the hull-propeller simulations, denoted HP1 and HP2 respectively.

Quantity	Notation	Unit	HP1	HP2
Velocity	V_0	m/s	1.60	1.773
Prop.rot.	n	1/s	7.53	8.92
Advance coef.	J	-	0.670	0.629
Trim	θ	^{o}	0.0	-0.2
Sinkage	Z	m	0.0	-0.0145

A cartesian coordinate system is used which has the origin at the stern of the hull. The x-axis is directed along the hull in the ship-forward direction with, $x = 0$, at the rudder stock. The y-axis is directed to the port side with, $y = 0$, on the symmetry plane of the hull. The z-axis is directed vertically upwards with, $z = 0$, at the propeller axis. In Figure 1b, the coordinate system is shown relative to the hull for the zero trim and sinkage condition of HP1. For the presentation of propeller results, we also use a polar coordinate system, (r, φ). The radius, $r = 0$, corresponds to the propeller axis and, $\varphi = 0$, corresponds to the vertically downwards direction. The angle increases in the direction of rotation of the propeller. The polar coordinate system is illustrated in Figure 1d.

METHODS

In this section, we briefly describe the main components of the complete algorithm used in this paper to compute the flow around the hull-propeller configuration under study. We also provide references to more complete presentations of the computational methods involved. Furthermore, the section includes information concerning mesh generation and other pre-processing of the simulations.

Large-eddy simulation

The conventional way of deriving the LES equations is to apply a low-pass filtering operation to the incompressible Navier-Stokes equations. Neglecting the terms stemming from the fact that, generally, differentiation and filtering do not commute, we obtain,

$$\begin{aligned} \frac{\partial \overline{\mathbf{v}}}{\partial t} + \nabla \cdot (\overline{\mathbf{v}} \otimes \overline{\mathbf{v}}) &= -\frac{1}{\rho} \nabla \overline{p} + \nabla \cdot (\overline{\mathbf{S}} - \mathbf{B}) \qquad (1) \\ \nabla \cdot \overline{\mathbf{v}} &= 0 \end{aligned}$$

where $\overline{\mathbf{v}}$ is the (filtered) velocity field, ρ the density, $\overline{p}$ the pressure, $\overline{\mathbf{S}} = 2\nu\overline{\mathbf{D}}$ the viscous strain tensor, $\overline{\mathbf{D}} = \frac{1}{2}(\nabla\overline{\mathbf{v}} + \nabla\overline{\mathbf{v}}^T)$ the rate of strain tensor, and ν the kinematic viscosity. The term in equation (1), arising from the filtering, is the subgrid stress tensor $\mathbf{B} = \overline{\mathbf{v} \otimes \mathbf{v}} - \overline{\mathbf{v}} \otimes \overline{\mathbf{v}}$. Here, variables with overbar denote filtered quantities. We refer to Sagaut (2002) as a general reference for LES and Fureby (2008), and the references therein, for LES applied to problems in naval hydrodynamics.

The LES modelling consists of deriving a computable expression for $\mathbf{B}$. The main models we have employed in the simulations presented below is the One Equation Eddy Viscosity Model (OEEVM) by Schumann (1975) and implicit LES. The OEEVM consists of an additional transport equation for the subgrid kinetic energy k,

$$\partial_t k + \nabla \cdot (k\overline{\mathbf{v}}) = \nabla \cdot (\nu_{tot} \nabla k) + 2\nu_k \|\overline{\mathbf{S}}\|^2 - \varepsilon.$$

Here $\nu_k = c_k \Delta \sqrt{k}$ (with c_k=0.07 and where Δ is the filter width), $\nu_{tot} = \nu + \nu_k$, and the dissipation $\varepsilon = c_\varepsilon k^{3/2}/\Delta$ (with c_ε=1.05). The subgrid stress is then computed as $\mathbf{B} = -2\nu_k\overline{\mathbf{D}}$. The implicit LES relies on the numerical diffusion to mimick the subgrid action of the turbulence, see e.g. Grinstein et al. (2007). In these simulations we

have used a mixed formulation of the subgrid stress term following Bensow and Fureby (2007). Several validation examples of these modelling techniques can be found in Fureby (2008). In the remaining sections of the paper, we drop the overline notation for filtered quantities.

In LES for ship hydrodynamics, even at model scale, it is necessary to apply near-wall modelling (NWM) instead of resolving the largest turbulent structures in the turbulent boundary layer, as these become gradually smaller as the hull is approached. An LES-approach to the turbulent boundary condition would lead to grid resolution requirements which increase faster with increasing Re-number for the boundary layer than for the turbulent regions away from the walls (Chapman, 1979). Such NWM is typically based on statistical arguments together with the mean velocity profiles of the viscous sub-layer and the logarithmic region of the turbulent boundary layer (Piomelli and Balares, 2002). The majority of these methods require the mean wall shear stress to be specified and used to adjust the velocity boundary condition. We, however, use a method which modifies the subgrid viscosity close to the wall, as described in Fureby et al. (2004).

The basis is the filtered boundary layer equations, which through the simplification of assuming zero streamwise pressure gradient and convective transport, integrate analytically to the logarithmic law-of-the-wall. This relation is the used to modify the subgrid model by adding a subgrid wall viscosity, ν_{NW}, to the kinematic viscosity so that the effective viscosity becomes,

$$\nu + \nu_{NW} = \tau_w/(\partial v/\partial y)_P = u_\tau y_P/v_P, \qquad (2)$$

where the subscript P denotes evaluation in the first cell center next to the wall, y is a local wall-normal coordinate and v is the tangential velocity component. In equation (2), the friction velocity, u_τ, is obtained either from the log-law or, preferably, from Spaldings law of the wall which incorporates also the buffer layer. Since the models only direct influence is on the subgrid viscosity, it can be combined with any other subgrid model.

The finite-volume method and the pressure-velocity coupling

The governing equations are discretised using the finite volume method and the unknown flow variables are stored in the cell-center positions in the computational grid. The algorithm supports arbitrary polyhedral cells and the grid is treated as unstructured. The approximations involved are of second-order accuracy, except for flux limiting for the convective term, which reduces locally the formal order of accuracy near sharp gradients. The momentum equation is treated in a segregated manner, solving sequentially the three components of the momentum equations in a loop within each time step. The coupling between the velocity and the pressure fields is handled with the PISO-algorithm (Issa, 1984). As the blade tip velocity imposes a Courant number (Co) restriction that is not directly related to the turbulent flow time scales, the HP2 simulation has been run with the so called PIMPLE algorithm in OpenFOAM, allowing for stable transient simulations with $Co \geq 1$ (in this case the maximum $Co \approx 2.5$). The PIMPLE algorithm is a merge of the SIMPLE (Patankar and Spalding, 1972) and PISO algorithms, where the PISO loop is complemented by an outer iteration loop and possible under-relaxation of the variables, see e.g. Barton (1998) for different ways to merge PISO and SIMPLE procedures.

The simulations are time resolved and a second order backward differencing scheme is used for the time advancement of the components of the momentum equation, as well as for the time advancement of possible additional transport equations associated with the sub-grid modelling described below. A domain decomposition technique, applied to the grid, in combination with an efficient MPI-implementation is used for running on parallel computers. The solvers which are used are implemented using the open source software package OpenFOAM, which provides an object-oriented library, based on the finite-volume method, specifically designed for CFD. See Weller et al. (1997), for a description of the structure of this software design.

Dynamic grid methods

The inclusion of a moving component (in this case the propeller) is significantly more complex from an algorithmic point of view as compared to fixed grid simulations. A number of approaches has been developed, and they can broadly be grouped into three classes; (i) Dynamic-grid methods, based on some form of re-meshing of parts of the computational domain; (ii) Sliding-interface methods; (iii) Overset-grid, or Chimera, methods (Chesshire and Henshaw, 1990). In the present work, two different methods, of type (i) and (ii) respectively, have been applied and in this section they are briefly described. More information concerning the special mesh generation procedures required are give below in the section describing the pre-processing of the hull-propeller simulations.

A dynamic mesh method, which has been developed at FOI, is applied in simulation HP1. It is based on deformation and regeneration (referred to as D&R) of the boundary-fitted computational grid, to account for the propeller motion. The D&R-method, its implementation, parallelization and application to hull-propeller simulation, is described in detail in Liefvendahl and Troëng (2007, 2008). The D&R-method is general, but here we indicate how it is applied to the hull-propeller simulations under study, see also below for information regarding the mesh generation. The computational domain is divided into three separate regions which are meshed individu-

ally. The first region contains the main part of the flow region around the hull, and here the grid is fixed throughout the simulation. The second region is a small cylinder surrounding the propeller, and here the grid rotates as a rigid body with the propeller. These two regions are connected with a third region in which the mesh is deformed during the motion, and regenerated at regular time intervals when the mesh distortion becomes large.

For HP2, the sliding-interface implementation recently introduced in OpenFOAM has been used, where in this case a cylindrical region enclosing the propeller is introduced, which rotates rigidly with the propeller, and interpolation is performed between the non-conforming sliding interfaces between the two regions. The implementation is based on the interpolation algorithm by Farrell and Maddison (2011), denoted as AMI (Arbitrary Mesh Interface). This constitues and efficient and conservative interpolation between non-conforming mesh interfaces based on Galerkin projection. The AMI has been shown to show good performance regarding both scalability and conservation of the flow quantities (Bensow, 2013, Turunen, 2014).

Mesh generation

For the D&R-simulation HP1, the division of the computational domain into three sub-regions is illustrated in Figure 2. The fixed grid around the hull consists of hexahedral (hex) cells. The propeller grid consists of tetrahedral (tet) cells, and a number of layers of prismatic (prism) cells for the boundary layer. The transition region is meshed with tet cells. When merging together the regions with different cell types, there arises polyhedral (poly) cells adjacent to the interface between the subregions. The number of cells of different type is given in Table 3.

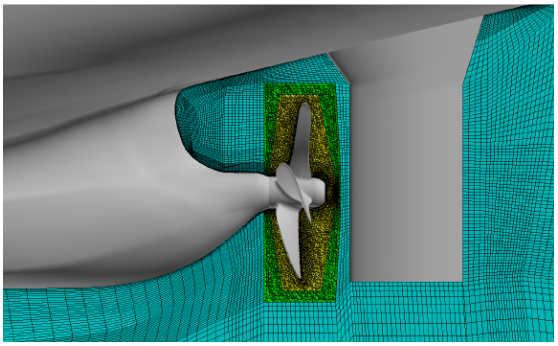

Figure 2: Illustration of the mesh regions of the D&R-algorithm applied to simulation HP1. Yellow indicates the grid which moves as a rigid body with the propeller, blue indicates the fixed grid around the hull, and green indicates the transition region where the mesh is deformed and regenerated.

Table 3: Number of cells in the computational grids, according to cell-type.

#cells/10^6	HP1	HP2
Hex	5.79	1.25
Tet	1.78	12.41
Prism	0.19	5.82
Poly	0.02	0.14
Total	7.77	19.63

For the sliding-interface simulation HP2, a primarily unstructured mesh apporach was adopted, except around the propeller. Here, two subregions are used, one fixed for the hull and one rotating cylinder around the propeller; the latter indicated by the red box in Figure 3. To achieve a well controlled resolution around the propeller, a structered hex mesh was first created around the blades, then the rest of the rotating cylinder domain was filled with unstructed tet elements, interfaced by pyramid elements (listed as polyhedral in Table 3). For the hull, a triangular surface mesh was created from which a prismatic boundary layer mesh was extruded before the rest of the domain was filled with tet elements.

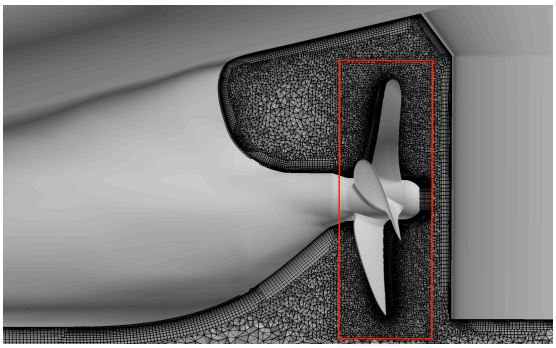

Figure 3: Illustration of the aft ship mesh for the simulation HP2, where the red box indicates the boundary of the rotating cylinder mesh where the sliding mesh interface is applied.

Other simulation parameters and pre-processing

The time advancement parameters, and pre-processing associated with force computation and pressure probes are described in this section. Table 4 summarizes the time step and the important time instants for simulations HP1 and HP2. Due to the very high computational cost of this type of simulations, it is necessary to create appropriate initial data for the simulations. This has been accomplished by simulating the hull flow, with the propeller effect modelled by an actuator disc (a force distribution). Since the geometrical propeller model is not included then, a time step which is an order of magnitude larger can be used for the simulation which provides the initial data. Still, when including the propeller, there is

a transient associated with this change. At time T_1, this transient effect on the propeller forces is deemed to have passed.

Table 4: Time advancement parameters. The time step, Δt, is given both in mikroseconds and degrees of propeller rotation. The start time of the simulation is denoted T_0, T_1 is the time instant when the start-up transients in the propeller forces have passed, and T_2 the end time of the simulation.

Quantity	HP1	HP2
$\Delta t(\mu s)$	9.2	15.6
$\Delta t(^o)$	0.025	0.050
T_0(s)	0.00	0.00
T_1(s)	0.55	0.48
T_2(s)	1.29	1.24
$(T_1 - T_0)/T_{rot}$	5.57	6.78
$(T_2 - T_0)/T_{rot}$	9.71	11.06

At each time step of the simulations, the fluid force and moment are integrated over certain areas (patches) of the hull, propeller and rudder surface. Each propeller blade corresponds to one patch, the propeller hub, the hull and the rudder constitute the remaining patches. The simulations thus provides the complete time history of these forces, including both viscous and pressure contribution. The moments are computed with respect to a point on the propeller axis.

Let $\mathbf{T}(S,t)$ denote the force on patch S at time t, and $\mathbf{Q}(S,t)$ the moment. For the propeller we include the blades, but not the hub, in the computation of propeller thrust and torque. If S_p denotes the propeller, then the conventional non-dimensional coefficients for thrust and torque are given by,

$$K_T(t) = -\frac{\mathbf{T}(S_p,t)\cdot\mathbf{e}_x}{\rho n^2 D_p^4}, \qquad K_Q(t) = \frac{\mathbf{Q}(S_p,t)\cdot\mathbf{e}_x}{\rho n^2 D_p^5}.$$

The unit vectors in the three coordinate directions are denoted by, $\mathbf{e}_x$, $\mathbf{e}_y$ and $\mathbf{e}_z$ respectively. Results will also be presented for the transversal and vertical forces on the propeller, for which we use the non-dimensional coefficients,

$$K_{Ty}(t) = \frac{\mathbf{T}(S_p,t)\cdot\mathbf{e}_y}{\rho n^2 D_p^4}, \qquad K_{Tz}(t) = \frac{\mathbf{T}(S_p,t)\cdot\mathbf{e}_z}{\rho n^2 D_p^4}.$$

For the axial load on an individual blade, we employ the corresponding coefficient,

$$K_{Tb}(t) = -\frac{\mathbf{T}(S_b,t)\cdot\mathbf{e}_x}{\rho n^2 D_p^4},$$

where S_b is the patch of the propeller blade.

Pressure probes on the hull above the propeller, were used in the experiments reported in Pecoraro et al. (2013). In the simulations we also include so-called probes, where the complete time-history of the pressure is saved. The probe placement and numbering is illustrated in see Figure 4, and it is the same in both simulations and experiments.

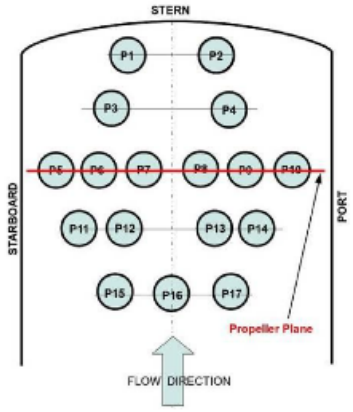

(a)

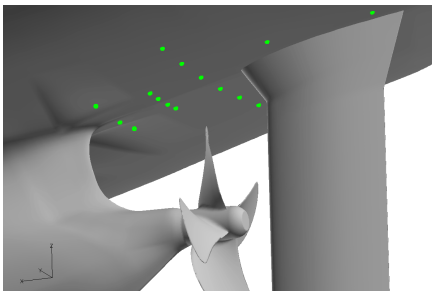

(b)

Figure 4: Placement and numbering of hull pressure probes. (a) Schematical drawing illustrating the numbering of the probes. (b) Illustration of the probe placements (green points).

THE TOWED HULL

Results from two large-eddy simulations, with different mesh refinement level, of the towed hull (without propulsion), are presented in this section. The operational parameters of these two simulations were the same as for simulation HP1, with a velocity, $V_0 = 1.6$ m/s, and zero trim and sinkage. Further information concerning the simulations are summarized in Table 5. The coarse mesh simulation is referred to as H1, and the fine mesh simulation is referred to as H2.

Table 5: Mesh size, time step and LES subgrid model for the hull simulations H1 and H2.

	H1	H2
#cells/10^6	4.9	14.6
Δt(ms)	0.15	0.10
LES-model	OEEVM	OEEVM

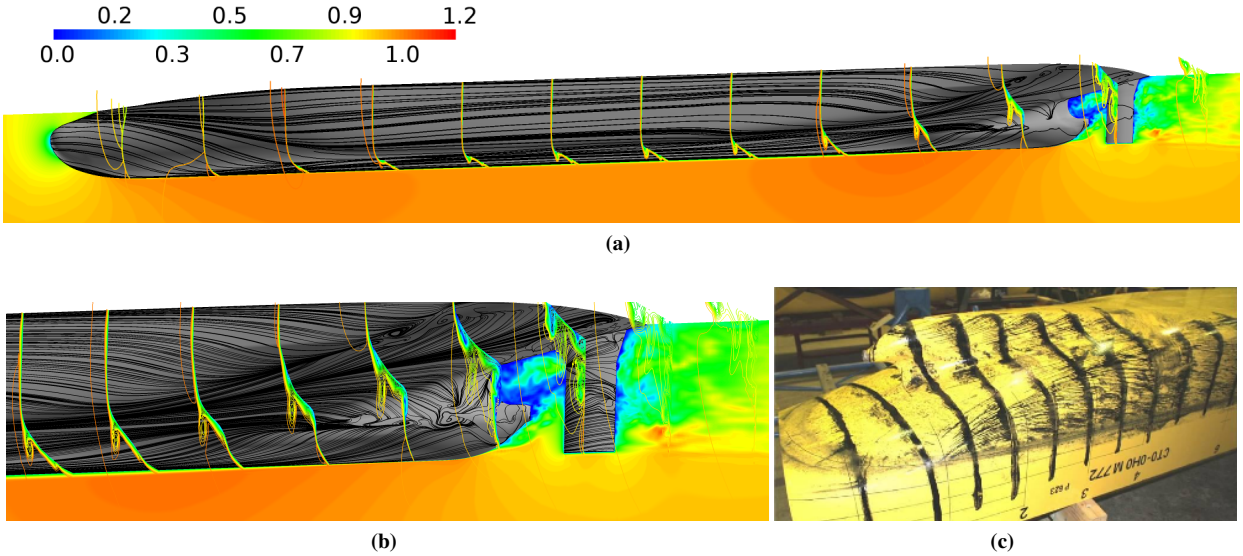

(a)

(b) (c)

Figure 5: Overview of the flow for the towed hull. In (a) and (b), the normalized instantaneous axial velocity from simulation H2 is plotted on the center plane and in cross-planes. Furthermore, the surface streamlines, also based on instantaneous velocity, are shown in black. The same quantities are shown in (a) and (b), with (b) being a zoom-in on the stern region. For (b), the density of surface streamlines has been increased, as well as the number of cross-plane velocity plots. (c): Paint visualization from towing tank experiments, of the hull surface flow in the stern region.

The mesh generation approach used when constructing the grids for simulation H1 and H2 is the same as that used for constructing the hull grid of simulation HP1. Hence the H1 and H2 grids contain exclusively finite volume cells of hexahedral type and the distribution and refinement of the grid is similar between H1 and HP1.

With a view to conditions of importance for propeller operation, we now provide an overview of the flow around the towed hull. In Figure 5, we show vizualisations of the flow based on simulation results from H2 and paint flow from towing tank experiments reported in Pecoraro et al. (2013). Along the hull, the flow is dominated by the pair of bilge vortices which are formed at the bow, extend along the hull, and separate slightly at the stern, passing well on the sides of the propeller disc. At the stern the flow becomes more complex as the adverse pressure gradient, caused by the hull curvature, decelerates the flow and a region of low flow velocity is created. Embedded into this region is the bilge vortex pair, as well as additional vortices created in the stern region. These vortices are indicated by surface streamline convergence in Figure 5.

The simulations indicate a shallow but significant unsteady flow separation on the hull after-body, just upstream of the propeller. The predicted extent of this region is quite similar for both H1 and H2. Furthermore, the shape and length scale of the largest shed structures is also qualitatively similar between H1 and H2. For simulation H2 the flow separation is slightly less pronounced. However, the finer grid employed in H2 also allows for the representation of smaller flow structures in the flow separation region, as compared to what is the case for simulation H1. The impact of these differences is most clearly seen in the nominal wake as described below. Overall, the occurence, shape and size of the flow separation predicted by the simulations is in accordance to the findings and analysis based on the towing tank experiments (Pecoraro et al., 2013). This holds also for the development and position of the bilge vortices and the flow over the gondola. Hence this provides validation of the large-eddy simulations and furthermore demonstrates that even the coarser grid used in H1 is sufficient to capture the largest features of the flow separation.

The most important aspect of the towed case for propeller operation is the nominal wake, i.e. the flow in the propeller plane with no propulsion. In Figure 6, both the mean and instantaneous nominal wake predicted by H1 and H2 are shown, as well as the measured mean nominal wake. The mean flow is computed based on time averaging during 7 seconds, which corresponds to approximately two hull flow-pass times ($T_{fp} = L_{PP}/V_0$). The main difference between the mean nominal wake for H1, as compared to H2, is in the upper region of the plots, around $(r, \varphi) \approx (R_p, 180^o)$. The flow here is complex and is affected by the decelation and the flow separation. Upstream of this region is the location of the largest discrepancy in flow-separation prediction between H1 and H2. We note that with respect to this, the fine grid simulation most resembles the measured nominal wake.

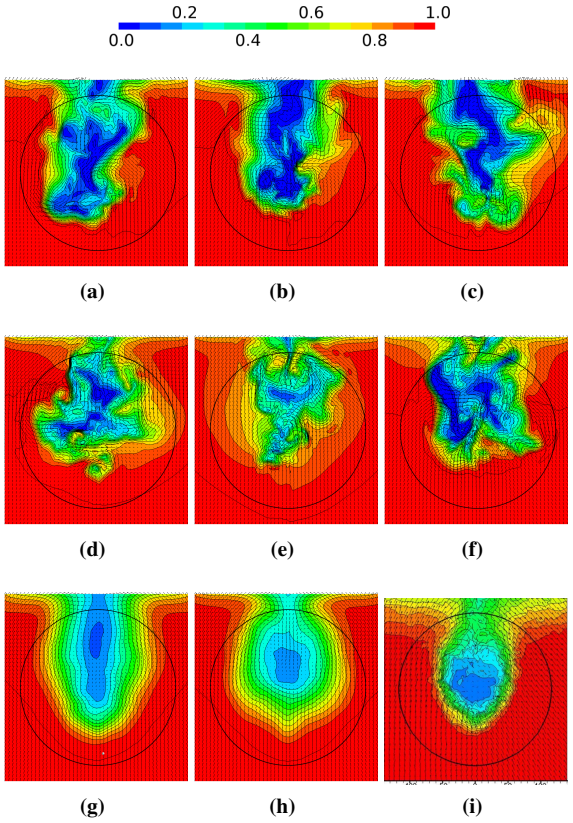

Figure 6: Nominal wake illustrated by a color plot of the axial velocity and black cross-plane vectors showing the transversal velocity component. (a-c) Results from simulation H1 based on the instantaneous velocity. (d-f) Results from simulation H2 based on the instantaneous velocity. (g) Mean velocity distribution for H1. (h) Mean velocity distribution for H2. (i) Mean velocity measured in towing tank.

The largest discrepancy between the measured and the computed mean nominal wakes concern the radial gradient of the axial velocity. The region with low mean axial velocity, say, $\langle v_x \rangle < 0.2V_0$, has a similar extent and shape between measurements and H2. The region with, $0.2 < \langle v_x \rangle / V_0 < 0.7$, on the other hand, is wider for H2 as compared to the measurements. This probably indicates that the flow separation region is slightly larger for the simulations than what is measured.

For the discussion of hull-propeller interaction further on, we also note the vertical component of the wake, due to the flow development over the gondola. There is a reasonable agreement between both simulations and the experiments regarding this flow component and it is the explanation to several features regarding the propeller behaviour discussed below.

The instantaneous nominal wakes, shown in Figure 6(a-c) for H1 and in Figure 6(d-f), are produced for arbitrarily chosen time instants well separated in time (with more than one second in between). The strong unsteadiness, mainly caused by the flow separation, is very apparent. Another aspect which is clear when comparing the instantaneous and mean nominal wakes is the limited use of the nominal wake for propeller design. The varying local flow that the propeller blades meets during the rotation is quite different than what is indicated by the mean nominal wake. This aspect will be discussed further below in connection with the discussion of the computed time-histories of the propeller blade loading.

THE PROPELLER IN OPEN-WATER CONDITION

The exact experimental configuration of the open-water test has not been reported. Normally, such a propeller test in a towing tank would be expected to be run with the propeller mounted upstream the shaft. As the geometrical details for the test are not known to us, the corresponding open-water simulation was set-up based on the self-propulsion configuration by using the same hub and cap and extending the shaft upstream. The simulated propeller thus operates pushing. We remark that the primary objective of the simulation is for qualitative comparison with the propeller operating in behind condition, and not to validate the computational technique. For this purpose we refer to Bensow and Liefvendahl (2008).

In this work, the only open-water simulation presented is for advance coefficient, $J = 0.629$, which is the experimentally determined (through thrust identity) operating condition corresponding to the self-propulsion case at, $V_0 = 1.773$ m/s. The simulation was performed using a mesh that around the propeller is indentical to the one used in the self-propulsion simulation HP2. The blade wake is somewhat refined in the open-water case which is not expected to significantly alter the behaviour compared with the grid used in the self-propulsion simulation. The thrust and torque for the simulation are reported in Table 6 and they are in good agreement with experimental data. The flow around the blade is discussed in connection with the behind condition below.

Table 6: Propeller thrust and torque in open water condition. Results from experiments and simulation P1.

$J = 0.629$	Exp.	P1
K_T	0.246	0.247
K_Q	0.406	0.411

THE COMPLETE HULL-PROPELLER CONFIGURATION

After the analysis above of the towed hull and the propeller in open-water condition, we now come to the main focus of the present paper: An analysis of the hull-propeller interaction, mainly based on results from simulations HP1 and HP2. We start by a discussion of the inflow to the propeller and a comparison between the propelled case and the towed case. The resulting mean forces and level of fluctuations of the forces on the propeller for the two simulated cases are then given. After this follows a detailed investigation of the blade load time histories and how to correlate this with the hull-propeller flow. We also consider the unsteady propeller dynamics, by analysing the flow around the blades at different loading condition, including a comparison with the open-water condition. The section is concluded with information from the pressure probes on the hull above the propeller.

The flow in the vicinity of the propeller

The structure of the inflow to the propeller, which is strongly affected by the flow separation upstream of the propeller, was discussed in connection with the analysis of the towed case. The inclusion of the propller leads to an accelation of the flow upstream of the propeller, and a contraction of the low velocity region. The effect is rather localized and significant only within approximately one propeller radius upstream of the propeller plane. Hence the flow separation upstream of the propeller is still present in simulations HP1 and HP2. The inflow to the propeller is illustrated in the cross-plane plots of Figure 7 which include results from one towed case (H1) and the two propelled cases (HP1 and HP2). Also shown in the figure is the velocity distribution just downstream of the propeller. The comparison is carried out using instantaneous data since no phase-averaging was included in the hull-propeller simulations for three-dimensional flow data. Naturally, there is a significant variation between instantaneous velocity distributions, but Figure 7 still provides an adequate illustration of the qualitative flow features discussed next.

First we compare the axial velocity shown in Figure 7a, simulation H1, with that in Figure 7c, simulation HP1. The operational parameters, the mesh generation approach and the subgrid modelling are the same between simulations H1 and HP1. Hence it is the propeller effect which is responsible for the difference. The flow acceleration and contraction of the flow velocity region, due to the propulsive effect, is clearly seen. Next we compare the axial velocity shown in Figure 7c, simulation HP1, with that in Figure 7e, simulation HP2. As described above, between HP1 and HP2, there is a slight difference in the operational parameters, different mesh generation approaches has been used and different subgrid modelling. The combined effect of these differences for the inflow to the propeller is that HP2 exhibits a smaller low velocity region than HP1. This is mainly due to the fact that a narrower flow separation region is predicted for HP2. The location and the qualitative features of the separation region are still quite similar, but the spatial extent is smaller for HP2 than for HP1.

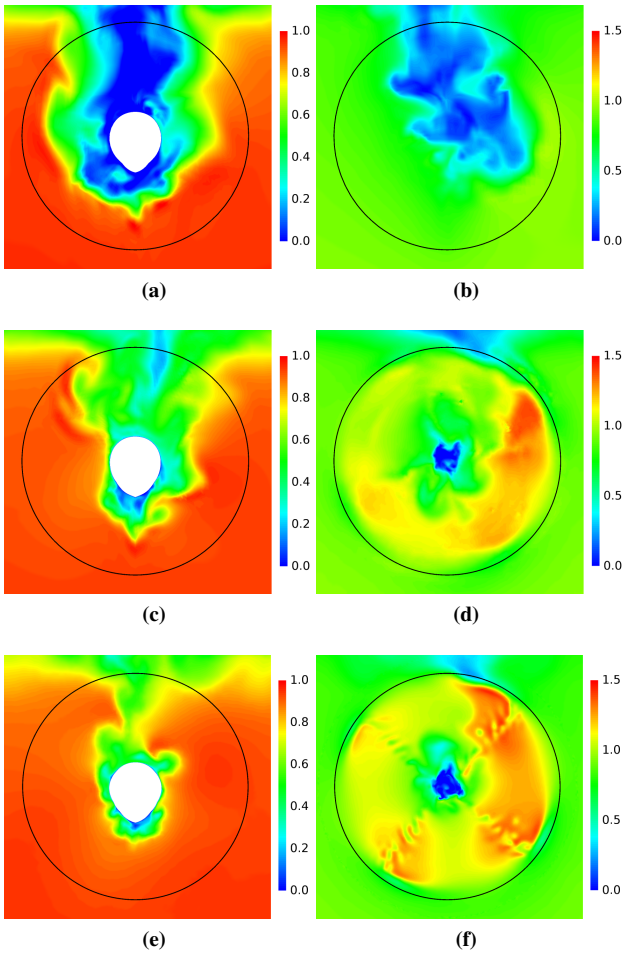

Figure 7: Instantaneous normalized axial velocity. In the left column (a,c,e); a cross-plane just upstream of the propeller at, $(x-x_p) = 0.514R_p$. In the right column (b,d,f); a cross-plane just downstream of the propeller at, $(x-x_p) = -0.342R_p$. Top row (a,b); the towed case, simulation H1. Middle row (c,d); simulation HP1. Bottom row (e,f); simulation HP2. The black circles illustrate the propeller radius. Observe that one color scale is used in the left column of pictures, and another in the right column of pictures.

The difference between Figure 7d, simulation HP1, and Figure 7f, simulation HP2, concerning the flow just downstream of the propeller, can be directly correlated to the difference in propeller inflow. Note that the propeller occupies different angular position in the two plots. That

the axial velocity is higher on the starboard side is mainly associated with the fact that there is a mean vertical component of the inflow to the propeller, which leads to higher blade load (and more flow acceleration) on the starboard side where the blade meets the vertical flow component. The finer grid resolution used in HP2 can also be observed in Figure 7f, where the blade wakes are clearly visible.

Propeller forces

Statistics for the propeller thrust, torque and transversal forces, as well as the blade loads, are summarized in Table 7 for simulations HP1 and HP2. The mean and the standard deviations have been calculated based on force time series of the last five rotations in each simulation. We use $\langle\cdot\rangle$ to denote the mean of a quantity, and $\sigma(\cdot)$ for the standard deviation.

Table 7: Propeller forces and torque. Total value given, including both pressure and viscous contribution. The experimental data is taken from towing tank measurements at, $V_0 = 1.6$ m/s. The definitions of the force coefficients are given in the preprocessing section.

	Mean			Std.dev	
	Exp.	HP1	HP2	HP2	HP2
K_T	0.237	0.232	0.247	0.012	0.007
$10K_Q$	0.398	0.388	0.396	0.014	- - -
K_{Ty}	- - -	0.001	-0.004	0.003	0.002
K_{Tz}	- - -	0.029	0.022	0.003	0.008
K_{Tb}	- - -	0.058	0.062	0.020	0.015

The computed mean thrust and torque show good agreement and are within 5% of the measured values for both simulations. The predicted thrust fluctuations, $\sigma(K_T)/\langle K_T\rangle$, are at 5.2% for HP1 and 2.8% for HP2. This difference is not unexpected considering the more unsteady inflow for HP1 (see Figure 7). The blade load fluctuations, $\sigma(K_{Tb})/\langle K_{Tb}\rangle$, naturally are significantly higher than the thrust fluctuations, and we have 34% for HP1 and 25% for HP2. Another important observation in Table 7 is the significant mean vertical force component on the propeller. This is caused by the sloping hull above the propeller and the resulting inclination of the propeller inflow. For HP1 the prediction is, $\langle K_{Tz}\rangle/\langle K_T\rangle \approx 12\%$, and for HP2 it is 9%. As elucidated below, this vertical force component is directly connected to the blade load variation during the rotation.

The blade load, K_{Tb}, is plotted as a function of rotation angle in Figure 8, for both HP1 and HP2. Both the phase average and the instantaneous blade load curves are included. The qualitative behaviour of the phase-averaged curve is explained by variation of the axial velocity of the inflow (see Figure 7) and the fact that there is a mean vertical component of the inflow to the propeller. The lowest blade load occurs at, $\varphi \approx 70^o$, where the blade rotates upwards and the axial flow velocity is relatively high. The highest blade load occurs in the vertical postion, $\varphi = 180^o$, or just after this, where the axial inflow velocity is very low. During the rotation from, $\varphi = 180^o$, to, $\varphi = 360^o$, the blade load falls off. Due to the vertical component in the inflow, there is a plateau with relatively high load with the blade to the starboard side, approximately in the interval, $200^o < \varphi < 330^o$.

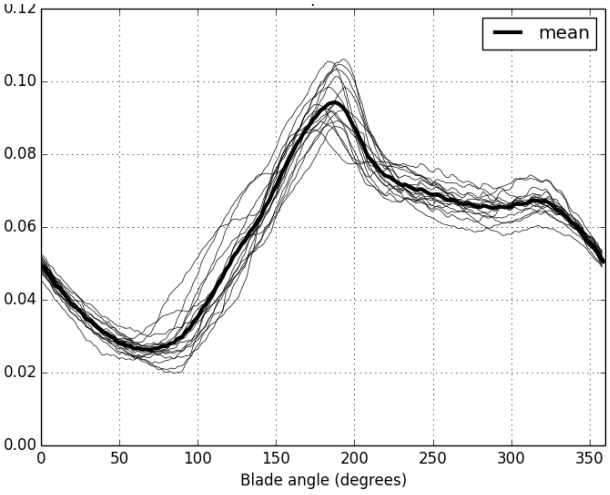

(a)

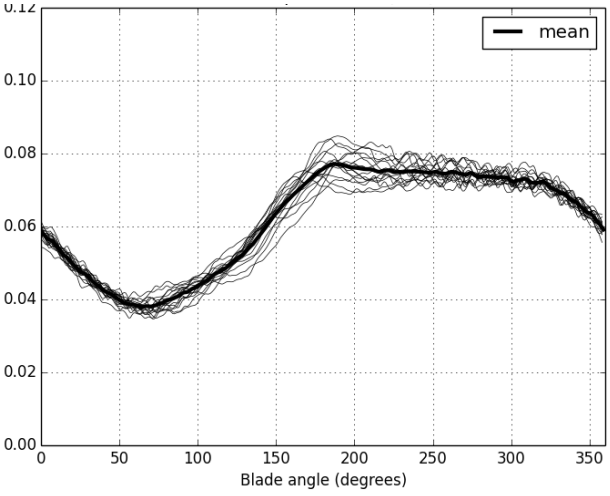

(b)

Figure 8: Scatter plot of blade load, $K_{Tb}(\varphi)$, based on data for four blades and four propeller rotations. The bold line represents the phase-averaged blade load. (a) Simulation HP1. (b) Simulation HP2.

Connecting this behaviour to vibrational considerations in the ship design, we note both pulsating component due to the large variation in blade thrust from the minimum position around $\varphi \approx 70^o$ to the maximum at $\varphi = 180^o$. Moreover, the propeller shaft will experience an average torque towards port due the plateau in the

thrust generated as the blade moves downward. This is visually also clear from Figure 7d and 7f.

Comparing the blade load curves for HP1 and HP2 in Figure 8, we see that there is larger variation during the rotation for HP1. This has two causes; (i) As shown above, the flow separation region upstream of the propeller is somewhat larger for HP1 than for HP2; (ii) As discussed in connection with Table 7, there is a larger vertical force on the propeller for HP1, this is reflected in the higher rise in K_{Tb} up to the peak. The unsteadiness of the inflow leads to shifts in both amplitude and phase of the load curve from cycle to cycle. In Figure 9, the time history of the thrust, K_T, is shown for both HP1 and HP2.

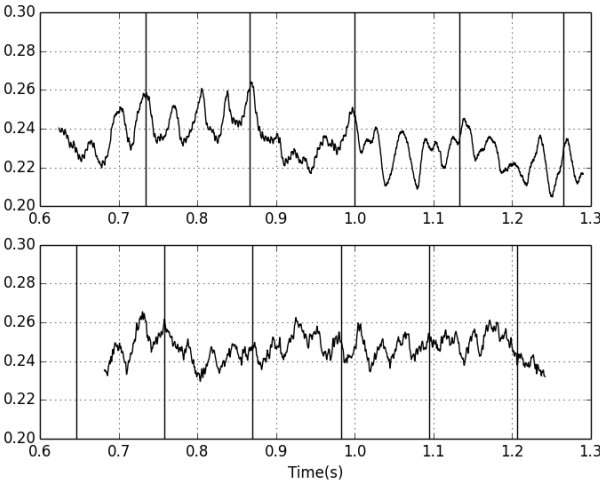

Figure 9: Plot of the thrust, $K_T(t)$, for HP1 (above) and HP2 (below). The vertical lines indicate time instants when the reference blade occupies the position, $\varphi = 0$.

Unsteady propeller dynamics

The above discussion concerned primarily the statistics of the propeller forces, while we will here describe the flow field around a single propeller blade during one revolution in behind condition, and discuss the details of the blade-to-blade variation. The main variation is, as described above, due to the characteristics of the wake field from the hull, with the high velocity deficit in the top position and a slight overall vertical component as the fluid rises along the aft hull lines. In addition to this, we see the variation due to the wake unsteadiness, both with respect to its width and vortex content, as well as a slow movement from side to side.

In Figure 10, we relate the loading in behind condition to the open water characterstics of the propeller. At, $\varphi = 0^o$, the bottom blade position, the loading condition is closest to open water condition with the K_{Tb} approximately one fourth of the total thrust coefficient, corresponding to $J = 0.654$ (through thrust identity). The blade then proceeds towards a lighter loading as is experiences a vertical flow component in the wake flow. Minimum loading is experienced at around, $\varphi \approx 70^o$, before a step increase towards the peak in the maximum velocity deficit of the wake. Following that, we have above noted the plateau as the blade has moved out of the wake peak but instead is rotating towards the vertical flow component on the starboard side of the hull.

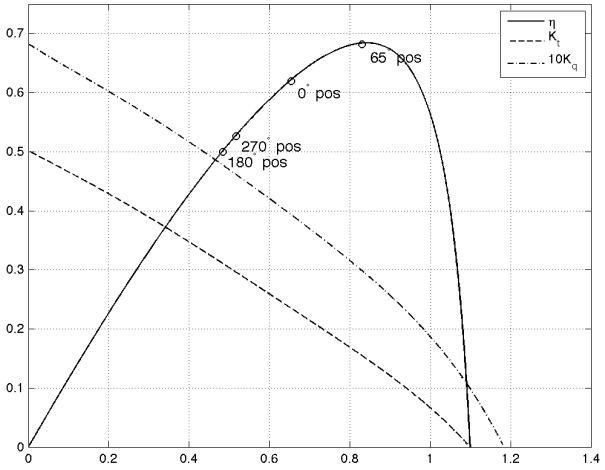

Figure 10: Phase average of blade load, at four selected angles, plotted in the open water diagram of the propeller. The points in the diagram represents the blade load multiplied by four, in order to correlate it with the thrust of the four-bladed propeller.

Finally, we conclude this section by a detailed discussion of the flow around the blades. The pressure field and surface streamlines on the blades are shown in Figures 11 and 12 for the positions at 0°, 90°, 180°, and 270°, of the self-propulsion simulation HP2 together with an instantaneous picture from the open water simulation P1. A general difference between the two conditions concerns the region of flow separation towards the trailing edge. This flow separation is present to some degree already in the open water condition, but is much more pronounced at all instances when the propeller operates in behind condition. We clearly see the traces of smaller vortical structures in the pressure field, and this behaviour is believed to be responsible for the small high frequency oscillations in the individual blade loading seen in Figure 8. The reason for this discrepancy is not fully understood at the moment, but could be related to the disturbed inflow and the time history of the blade loading.

Considering the blade in the vertically downwards position, the blade flow is as expected fairly similar to the open water condition, see Figures 11b and 11e. We note though that the low pressure region on the suction side tip of the blade is much shorter in the behind condition as the blade is moving towards the lighter loaded position. This is however compensated by higher pressure levels on the pressure side of the blade, giving the slightly higher

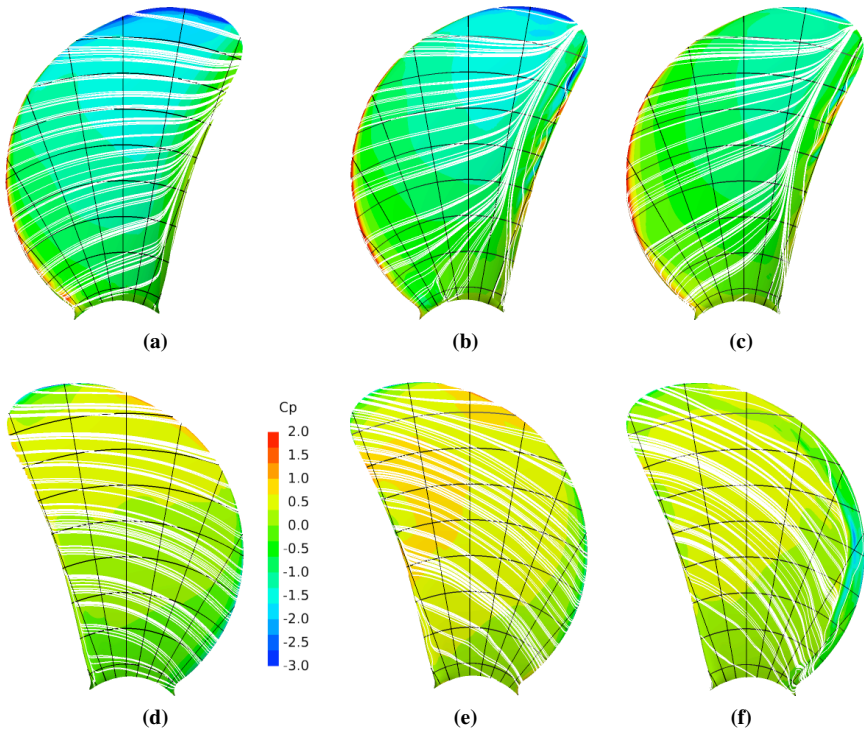

Figure 11: Contours of pressure coefficient, C_P, and surface streamlines. The suction side is shown in the top row of pictures and the pressure side in the bottom row. Figures (a) and (d): Open-water condition, simulation P1. Figures (b) and (e): Simulation HP2, blade vertically downwards, $\varphi = 0$. Figures (c) and (f): Simulation HP2, blade to port side, $\varphi = 90^o$.

loading compared with the open water condition. As the blade moves in the following wake on its way towards the top position, a dramatic difference is however developing on the pressure side where the leading edge is now covered by a rather large region of relatively low pressure. Moreover, the surface streamlines indicate the possible development of a pressure side vortex along the radii below, $r/R_P \approx 0.8$. Relating this behaviour to Figure 10, we can indeed see that the blade is operating very close to the efficiency peak, and will certainly during some rotations pass over the peak. This is in accordance with the flow behaviour noted above.

Towards the top position, the pressure level on the pressure side increases considerably and the pressure side vortex, noted at the port position, has disappeared. On the suction side, the thrust generating pressure is more concentrated towards the leading edge with a zone with very low pressure developing from, $r/R_P \approx 0.8$. In the starboard position, corresponding to the thrust plateau mentioned above, the pressure field once again approaches that of the open water condition, although with a higher pressure on the back side of the blade. We can also see how the surface streamlines are deflected by the thickening tip vortex that develops during the previous quarter of a revolution.

Returning to the cycle-to-cycle variation in thrust, this is related to the unsteady nature of the wake. Looking at Figure 8 again, we note two qualitatively different types of variations around the mean, apart from the small oscillations discussed above. The first is the variation in level in K_{Tb} primarily due to how large the velocity deficit in the wake is at that particular instant for the particular blade position. We here note a variation in the order of $\pm 15\%$. This is most pronounced for the peak load at the top position and to a large extent also at the plateau, but to some extent, surprisingly enough, also in the bottom position. We note however that the flow analysis above indicate intermittent separation also towards to lower part of the gondola entering then the bottom blade position.

The second type of variation is the phase shift of the curves in Figure 8, clearly seen between blade postions of about, $\varphi \approx 60^o$, and, $\varphi \approx 200^o$. This is related to the wake velocity deficit moving laterally, with the blade then experiencing the maximum loading during the revolution not exactly at the top position, but with a variation for each blade passage. An example of this behaviour is illustrated in Figure 13. Here, the axial component of effective wake entering the propeller during one revoultion of the HP2 simulation is illustrated; it is believed that the tangential components have little influence on this discussion. The variation in velocity deficit does here seem to follow from the vortex system close to the gondola. In Figure 13b,

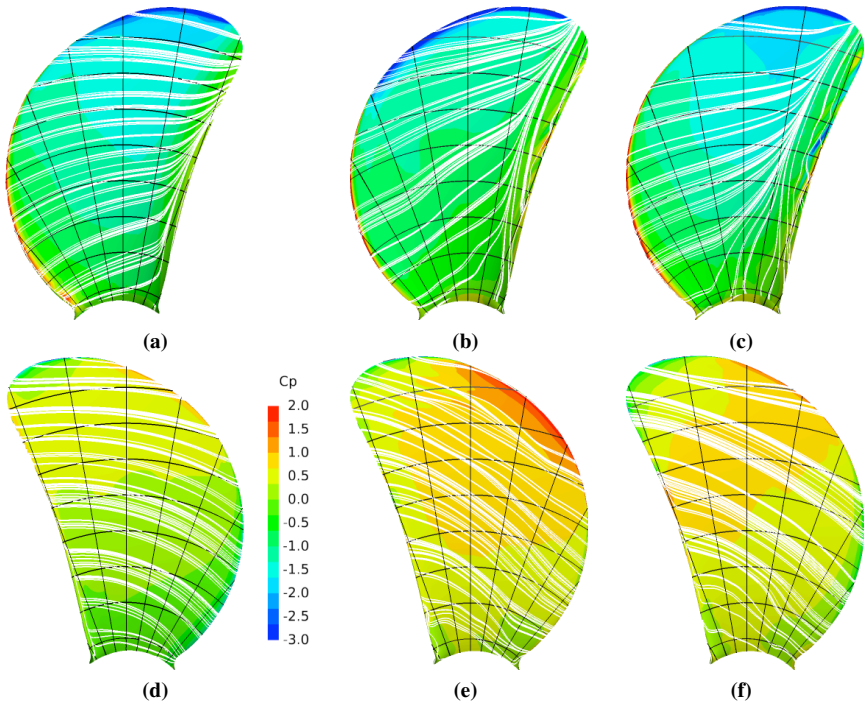

Figure 12: Contours of pressure coefficient, C_P, and surface streamlines. The suction side is shown in the top row of pictures and the pressure side in the bottom row. Figures (a) and (d): Open-water condition, simulation P1. Figures (b) and (e): Simulation HP2, blade vertically upwards, $\varphi = 180^o$. Figures (c) and (f): Simulation HP2, blade to starboard side, $\varphi = 270^o$.

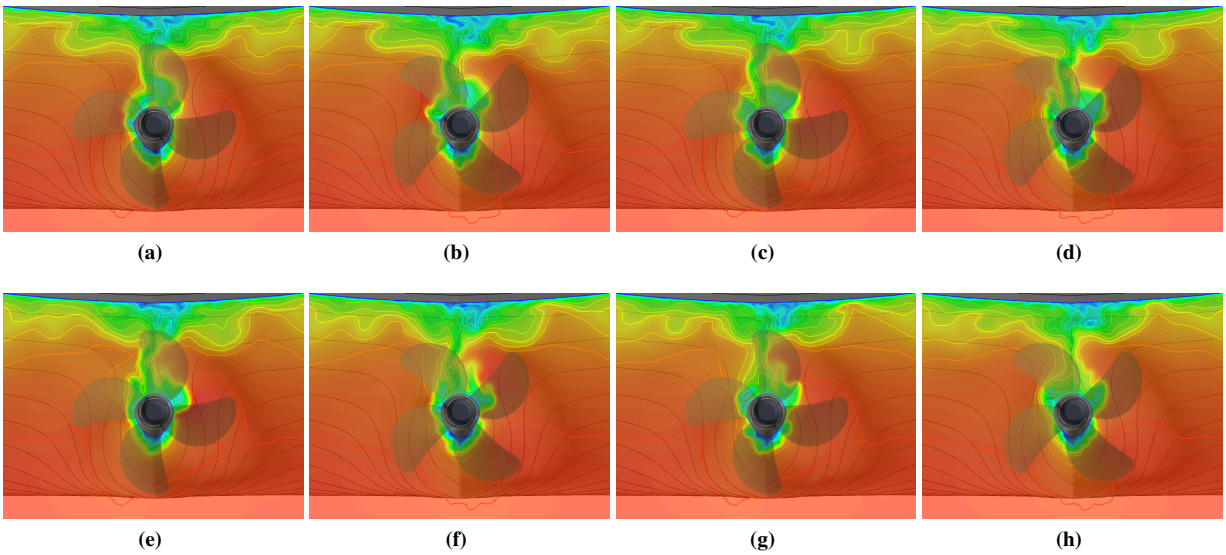

Figure 13: Wake inflow to the propeller during one revolution in simulation HP2. The figure shows instantaneous normalized axial velocity in a cross-plane just upstream of the propeller at, $(x - x_p) = 0.514R_p$, with the same colorscale as in Figure 7. Between the consequtive figures, the propeller rotates 45^o.

we note a low velocity region almost at the centreline at about, $x/R_P = 0.5$. In the following frames, this moves to the starboard side along the gondola. In frame (g), this flow structure seems to have passed. Instead, in the next frame, we see a new structure emerging on the port side, at approximately, $\varphi \approx 135^o$, which then more or less stays in this position for the rest of the revolution. From this visualisation it is easy to understand that the blade in top position in frame (c) experiences a higher loading than the top blade in frame (g), and also that the blade entering top position in frame (b) most likely already delivers a higher thrust than the top blade in frame (g).

The description here has been made for only one realisation of rotation, but it is clear from Figure 8 that the sequence here repeats itself for all rotations. This variation has largest impact on the blade as it moves upwards to the top position, However, we remark that the load peak also occurs over a range of propeller positions spanning, $\Delta\varphi \approx 25^o$, around the top position. The behaviour we see in these simulations, and illustrated in Figure 13, also indicates that the average wake width is considerably wider and smeared compared with the instantaneous, and that this is due to the constantly changing position of relatively thin flow structures in the instantaneous wake.

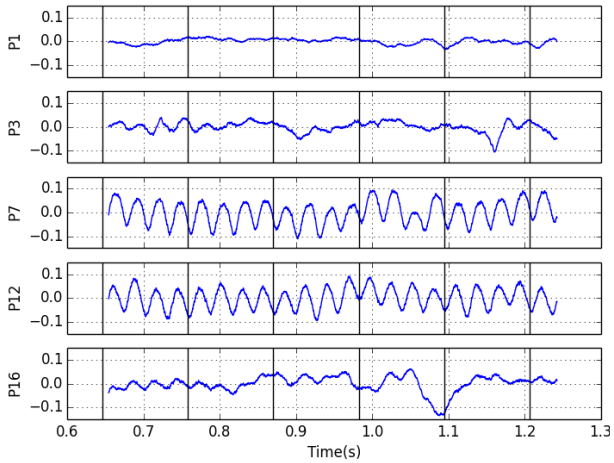

Figure 14: Time history, from simulation HP2, of the pressure coefficient in the probes 1, 3, 7, 12 and 16 respectively. The mean component has been subtracted from the signals. The vertical black lines indicate time instants when the reference blade occupies the position, $\varphi = 0$.

Hull pressure fluctuations

For both simulations, HP1 and HP2, the pressure time history is computed in 17 different probes placed on the hull above the propeller, as described in the section on preprocessing. Results are here presented in terms of the pressure coefficient based on the vessel velocity, $C_P = 2p/(\rho V_0^2)$.

As shown in Figure 4, the probes are placed in five rows with different axial (x-)coordinate. In Figure 14, the pressure signals, from simulation HP2, are shown for five selected probes, one from each row. The pressure fluctuations in the most upstream row of probes, represented by probe 16 in Figure 14, is mainly caused by the flow separation. For the next two rows of probes, represented by probe 12 and 7 respectively, the propeller action is the dominant source of pressure fluctuations. The most downstream probes are placed on the sides of the rudder. The signals for probe 12 and 7 are dominated by the periodic contribution at the blade frequency, but strong cycle-to-cycle variations are also apparent. The marked pressure minimum for probe 16 at, $t \approx 1.1$ s, is most likely associated with a transient flow separation. The standard deviation of the pressure probe data, for both simulations, is summarized in Figure 15.

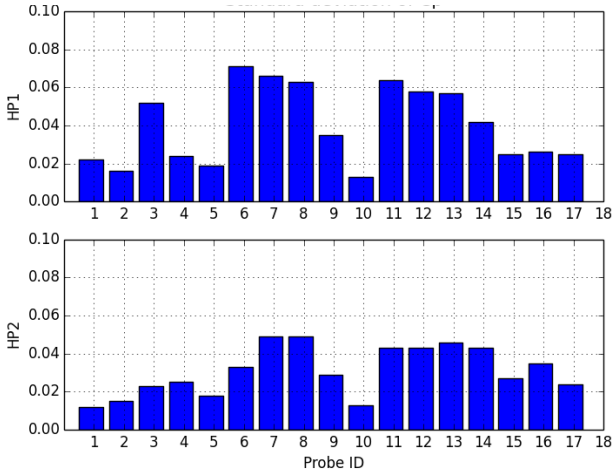

Figure 15: Standard deviation of pressure probe data, $\sigma(C_p)$, for simulations HP1 (above) and HP2 (below).

CONCLUSIONS

In this paper, we have presented results from several large-eddy simulations of a 7000DWT chemical tanker, with a flow analysis focusing on unsteady propulsor-hull interaction phenomona. All studies have been performed in model scale. The main results were produced in two simulations of the complete hull-propeller-rudder configuration, under slightly different operating conditions. A complete geometrical propeller model was included in these two simulations, using a dynamic grid method in simulation HP1 and a sliding interface method in simulation HP2. These simulations were complemented by simulations of the towed hull configuration and the propeller in open-water condition. A mesh sensitivity study was performed for the hull-only case. Comparison with experimental data was carried out for a number of flow quan-

tities, for the hull-only case, the open-water propeller, as well as for the hull-propeller case.

The simulations show good agreement with the experiments in cases with similar conditions and qualitatively display reasonable behaviour for other conditions. From the simulations, it is possible to extract detailed transient flow information to improve the understanding of how the propeller is influenced by the complex hull wake flow. For this hull in model scale, a disctinct flow separation zone is present just upstream the propeller, which a incurs a large variation in propeller blade loading, not only during one propeller revolution but also in between different blade passages. The separating flow is expected to decrease significantly in full scale, but this does not necessarily imply that the level of effective wake unsteadiness will decrease significantly. Full-scale investigations of the type illustrated in the present paper are expected to be feasible in the near future. An important feature in the wake flow is the vertical flow component into the propeller plane, significantly responsible for a high variation in blade load during one revolution, perhaps more so than the velocity deficit from the flow separation. A secondary of effect is the development of flow structures entering the blade root area.

With the current development of computational capacity, the type of analysis techniques illustrated in the present paper are becoming worthwhile to carry out prior to design in order to understand what flow features govern the propeller operation and the time-resolved behaviour. How to best support the design process with these new analysis tools is however yet to be elucidated, and the authors hope that the present paper can contribute to that developement. The simulations results presented in this work clearly illustrates that the instantaneous wake differs significantly compared with the average effective wake, and of course even more so for the nominal wake. This knowledge is relevant not only regarding design requirements on transient features, such as vibration, noise, and cavitation, but also influences integral quantities such as thrust and propulsive efficiency.

Acknowledgements

The authors wish to thank other partners of the STREAMLINE project involved in the investigation of the configuration under study, and its design optimisations, for fruitful scientific discussions concerning how complementary computational and experimental techniques can advance the understanding of unsteady hull-propeller interaction. In particular CNR-INSEAN, and Francesco Salvatore, have been most helpful in connection with the towing tank experiments.

This paper was partially supported with funding from the European Union 7th Framework Programme under project STREAMLINE (grant agreement number 233896).

REFERENCES

Barton, I. E. (1998). Comparison of SIMPLE- and PISO-type algorithms for transient flows. *Int. J. Num. Meth. Fluids*, 26.

Bensow, R. (2013). Simulation of unsteady propeller blade loads using openfoam. 16^{th} Numerical Towing Tank Symposium, NuTTS'13, Mülheim, Germany.

Bensow, R. and Fureby, C. (2007). On the justification and extension of mixed methods in LES. *J. Turbulence*, 8.

Bensow, R. and Liefvendahl, M. (2008). Implicit and explicit subgrid modeling in LES applied to a marine propeller. Number AIAA-2008-4144.

Calcagni, D., Bellotto, F., Broglia, R., Salvatore, F., and Bensow, R. (2014). Comparative analysis of the hydrodynamic performance of conventional and twisted rudders using a hybrid ranse/bem model. ISOPE 2014, Busan, Korea.

Chapman, D. R. (1979). Computational aerodynamics development and outlook. *AIAA Journal*, 17:1293–1313.

Chesshire, G. and Henshaw, W. D. (1990). Composite overlapping meshes for the solution of partial differential equations. *J. Comp. Phys.*, 90:1–64.

Deng, G. B., Queutey, P., Visonneau, M., and Salvatore, F. (2013). Ship propulsion prediction with a coupled RANSE-BEM approach. V International Conference on Computational Methods in Marine Engineering, MARIN2013, Hamburg, Germany.

Farrell, P. E. and Maddison, J. R. (2011). Conservative interpolation between volume meshes by local galerkin projection. *Comput. Methods Appl. Mech Engrg*, 200(89).

Fureby, C. (2008). Large Eddy Simulation of Ship Hydrodynamics. In *27th Symposium on Naval Hydrodynamics*, Seoul, Korea.

Fureby, C., Alin, N., Menon, N., Svanstedt, S., and Persson, L. (2004). On large eddy simulation of high reynolds number wall bounded flows. *AIAA Journal*, page 457.

Grinstein, F., W., L. M., and Rider, editors (2007). *Implicit Large Eddy Simulation: Computing Turbulent Fluid Dynamics*. Cambridge University Press, Cambridge, England.

Issa, R. I. (1984). Solution of the implicitly discretised fluid flow equations by operator-splitting. *J. Comp. Phys.*, 62:40–65.

Liefvendahl, M. and Troëng, C. (2007). Deformation and Regeneration of the Computational Grid for CFD with Moving Boundaries. In *45th AIAA Aerospace Sciences Meeting and Exhibit*, number AIAA-2007-1458.

Liefvendahl, M. and Troëng, C. (2008). Parallelization and Load Balancing of a Dynamic Mesh Method for Moving Boundary CFD. In *OpenFOAM International Conference*. Berlin, Germany.

Patankar, S. V. and Spalding, D. B. (1972). A calculation procedure for heat, mass and momentum transfer in three-dimensional parabolic flows. *Int. J. Heat Mass Transfer*, 15.

Pecoraro, A., Felice, F. D., Felli, M., Salvatore, F., and Viviani, M. (2013). Propeller-hull interaction in a single-screw vessel. In *3rd Int. Symp. Marine Propulsors*, Launceston, Tasmania, Australia.

Piomelli, U. and Balares, E. (2002). Wall-layer models for large-eddy simulation. *Annual Review of Fluid Mechanics*, 34:349–374.

Queutey, P., Deng, G. B., Guilmineau, E., and Salvatore, F. (2013). A comparison between full ranse and coupled RANSE-BEM approaches in ship propulsion performance prediction. 32nd International Conference on Ocean, Offshore and Artic Engineering, OMAE2013.

Sagaut, P. (2002). *Large eddy simulation for incompressible flows.* Springer-Verlag.

Schumann, U. (1975). Subgrid scale model for finite difference simulation of turbulent flows in plane channels and annuli. *J.Comp.Phys.*, 18(4):376–404.

Turunen, T. (2014). Analysis of multi-propeller marine applications by means of computational fluid dynamics. Master's thesis, Aalto University.

Van der Ploeg, A. and Foeth, E. (2013). Optimization of a chemical tanker and propeller with CFD. V International Conference on Computational Methods in Marine Engineering - MARINE2013, Hamburg.

Weller, H., Tabor, G., Jasak, H., and Fureby, C. (1997). A tensorial approach to CFD using object oriented techniques. *Comput. Phys.*, 12:620.